Random alloy nanoparticles of Pd and Au immobilized on reducible metal oxides and their catalytic investigation

Ali K. Ilunga, Reinout Meijboom*

Department of Chemistry, University of Johannesburg, P. O. Box 524, Auckland Park 2006, Johannesburg, South Africa

ABSTRACT

Well-dispersed, random alloy, palladium-gold nanoparticles (2.66 ± 0.51 nm) were immobilized onto several reducible mesoporous transition metal oxide materials. The composites (palladium-gold nanoparticles immobilized onto mesoporous transition metal oxide (PdAu–MTMO)) were characterized through several analytical methods such as UV–vis spectroscopy, BET, XRD, FT-IR, ICP-OES, TEM and TPR analyses. Catalytic oxidation of morin (quercetin) was performed as a model reaction in the presence of hydrogen peroxide to investigate the synergic catalytic activity of the composite. Silica was used as inert support to isolate the catalytic activity of the metal nanoparticles (32.69 ± 9.93 kJ mol^{-2}). Synergistic interaction of PdAu–MTMO was mechanically described according to Langmuir-Hinshelwood and Mars-van Krevelen approaches. The TOF of PdAu–Co$_3$O$_4$ (6073.23 ± 85.01 s^{-1} mol^{-1}) was considerably larger than that of random alloy nanoparticles (PdAu–SiO$_2$ (25.71 ± 2.35 s^{-1} mol^{-1})). The Arrhenius-type plot was constructed to determine the synergistic activity of the composite, where PdAu–Co$_3$O$_4$ described the best synergistic interaction.

© 2016 Elsevier B.V. All rights reserved.

1. Introduction

Since the Mobil Oil Corporation's discovery over 20 years ago, countless mesoporous materials were produced and considerable effort was applied to improve its physicochemical features [1,2]. Several types of mesoporous materials were reported based on the synthesis methods [3,4], the doping materials [5], and the composite materials [6]. The use of mesoporous materials expanded to a large scientific field based on their features [7,8]. The thermal stability described by most of the mesoporous materials increase their application in several industries such as manufacturing [9]. The tunable structural properties of mesoporous materials justified their interest in catalysis [10,11]. The mesoporous transition metal oxide (MTMO) materials demonstrated a wide catalytic potential in diverse oxidation and reduction reactions due to the multiple oxidation states of the transition metal [12].

A common synthesis approach of MTMO materials is conducted in an aqueous medium, which results in thermally unstable and amorphous wall materials [13,14]. Suib's group recently reported the synthesis approach of several mesoporous transition metal oxide materials using sol-gel chemistry in a non-aqueous solvent

[15]. The hydrolysis and condensation of oxo-clusters were controlled by NO$_x$ chemistry taking place *in situ* due to the thermal decomposition of nitrate ions [16,17].

The catalytic activity of palladium-gold random alloy nanoparticles encapsulated into dendrimer cavities was recently reported by our group [18]. The catalytic activity was investigated through morin oxidation as a model reaction in the presence of hydrogen peroxide. The adsorption isotherm of the reactants onto the alloy nanoparticles surfaces were investigated through the Langmuir-Hinshelwood mechanism which described the alloy nanoparticle activities relative to the alloy ratio and the optimization of their activities through the performed model reaction [18].

Here, we report the synthesis of several mesoporous transition metal oxide materials through the inverse micelle approach using nitrate ions to prevent condensation. It was reported that the heat treatment resulted in pore expansion of those mesoporous materials [15]. Therefore, the heat cycling was subdivided into four steps where 450 °C will be the last heat treatment temperature. The catalytic activity shown by mesoporous transition metal oxide materials was reported in a large number of investigations [19–22]. The synthesis of CeO$_2$, NiO, Fe$_2$O$_3$, Co$_3$O$_4$, MnO$_2$, and SiO$_2$ will be performed. The encapsulated random alloy (PdAu) nanoparticles will be immobilized on these mesoporous transition metal oxides. The catalytic oxidation of morin (natural flavonoid) will be performed as a model reaction [23,24]. A comparative evalu-

ation related to the catalytic activity of the mesoporous transition metal oxide materials and their supported alloy nanoparticles will be described to identify the most active combination. The catalytic process will be monitored through UV–vis spectroscopy by recording the absorbance peak at λ 410 nm (morin maximum absorbance) [25].

2. Experimental section

2.1. Mesoporous metal oxide materials

A generic inverse micelle approach developed by Suib's group was followed to synthesize the mesoporous metal oxide materials [15]. Tetraethyl orthosilicate (≥99.0%), manganese (II) nitrate tetrahydrate (≥99.0%), iron (III) nitrate nonahydrate (≥98.0%), cobalt (II) nitrate hexahydrate (≥98.0%), nickel (II) nitrate hexahydrate (≥99.0%), and cerium (II) nitrate hexahydrate (≥99.0%) (Sigma-Aldrich), were used as metal precursors. The oxo-cluster aggregation was prevented using the surfactant, Pluronic® P-123 (Sigma-Aldrich), as a nanoreactor. The surfactant was mixed with 1-butanol (Rochelle chemical, ≥99.5%) and nitric acid (Rochelle chemical, ≥55.0%). The metal salt was added to an acidified alcoholic solution of P-123 while stirring. The synthesis of cobalt oxide was conducted using 4.08×10^{-4} mol (2.37 g) of P-123 mixed with 0.23 mol (21.04×10^{-3} L) of 1-butanol. The mixture was acidified with 0.038 mol (2.29×10^{-3} L) nitric acid. Exactly, 0.02 mol (5.82 g) of cobalt nitrate hexahydrate was added to the acidified alcoholic solution. The gel solution was heated to 120 °C for 4 h under air. The obtained powder was washed with an excess of ethanol (Associated Chemical Enterprises, ≥95.0%), centrifuged and dried in a vacuum oven overnight at 60 °C. The heating cycle was subdivided into four steps proceeding to different temperatures 150 °C (12 h), 250 °C (4 h), 350 °C (3 h), and 450 °C (2 h), respectively. Prior to proceeding with the next heating cycle, the powder was cooled to room temperature. The reactant amounts used for the synthesis of CeO_2, NiO, Fe_2O_3, MnO_2, and SiO_2 is shown in Supporting information (Table 1S). Silica was calcined directly at 450 °C for 4 h, however, all the other materials were subjected to heating cycles.

2.2. Dendrimer encapsulated random alloy (PdAu) metal nanoparticles

The synthesis approach of the encapsulated random palladium-gold nanoparticles was adapted based on Crooks's report [26]. In light of our previous investigation, an optimal molar ratio of palladium-gold (alloy) nanoparticles ($Pd_{75}Au_{35}$/DENs-OH) was used to prepare the random alloy nanoparticles [18]. The fifth generation hydroxyl terminated poly(amido-amine) dendrimer was used as a template for the encapsulated random alloy nanoparticle synthesis. A stock solution of 10^{-4} M dendrimer (Dendritech®, 4.98 wt.% solution in methanol) contained in 15×10^{-3} L of deionized water was used as a template to encapsulate the random alloy nanoparticles. The methanol solution was removed *in vacuo* at room temperature. Exactly, a 75 molar ratio of palladium (potassium tetrachloropalladate, ≥98.0% (Sigma-Aldrich)) and a 35 molar ratio of gold (chloroauric acid, ≥99.9% (Sigma-Aldrich)) ions were added into the dendritic solution, respectively. To assure the interaction of palladium ions with the internal tertiary amine groups, the mixture was subjected to stirring for 30 min. An alkaline solution of sodium borohydride (≥98.0%, Sigma-Aldrich) was added to initiate the metal ion reduction. For an efficient reduction of the metal ions, the sodium borohydride was added in excess. The reduction of both metal ions complexed in the dendrimer structure resulted in the encapsulated random alloy nanoparticles [26]. Dialysis mem-

brane (Snakeskin® Dialysis Tubing (10,000 MWCO)) was used to remove the excess reducing agent.

2.3. Immobilization of random alloy nanoparticles onto mesoporous metal oxide

The immobilization of the encapsulated metal nanoparticles on the mesoporous metal oxide materials was performed following the Somorjai group's report [27]. The mesoporous metal oxide material was mixed with the encapsulated random alloy nanoparticle solution. The mixture was stirred for 30 min prior to sonication for 3 h using a digital ultrasonic cleaner (Celsius Scientific cc). The slurry was centrifuged at 15,000 rpm for 10 min (Lasec (HERMLE Labortechnik GmbH)). The precipitate was dried at room temperature for 2 days and heated at 100 °C in an oven for 4 h. The percentage of the palladium-gold nanoparticles immobilized onto the metal oxide pores were estimated through inductively coupled plasma optical emission spectrometry (ICP-OES) analysis in *aqua regia* medium [28]. The amount of alloy on mesoporous metal oxide materials range $(10–30) \times 10^{-3}$ g was mixed with 4×10^{-3} L of *aqua regia* ($HCl/HNO_3 = 3/1$ (v/v)) and diluted at 50×10^{-3} L of deionized water. The solution was filtered prior to analysis.

The mesostructure of the mesoporous transition metal oxide materials was evaluated through X-ray diffraction (XRD) analysis (Rigaku Mini Flex 600). The surface area, pore volume, and pore diameter were investigated by Brunauer–Emmett–Teller (BET) analysis (Micromeritics Tristar) based on isothermal adsorption and desorption of nitrogen gas onto the mesoporous metal oxide materials surface. Amounts of 0.1–0.3 g of each synthesized mesoporous material were degassed overnight prior to analysis. The metal-oxygen stretching vibration was analyzed through Fourier transformed infrared (FT-IR) analysis using FT-IR spectroscopy (Bruker Tensor 27). The micrograph analysis of mesoporous metal oxide materials was conducted using a high-resolution transmission electron microscopy (HR-TEM) (JOEL JEM–2100F electron microscope). Small quantities of mesoporous materials were diluted in ethanol and sonicated for 30 min. A copper grid was used to sample the solution and dried at room temperature prior to transmission electron microscopy analysis. The reducibility of the synthesized mesoporous metal oxide materials was evaluated by temperature programmed reduction (Micromeritics AutoChem II). Approximately 0.03-0.04 g of the synthesized materials (MTMO and PdAu–MTMO) was weighted and placed in the reactor to perform the temperature programmed reduction (TPR) analysis. The TPR analysis was performed using a gas composition of H_2-He, the temperature range was 50–900 °C where the heat flow rate was 10 °C min^{-1}.

2.4. Catalytic investigation

An aqueous morin (≥98.0%, Sigma-Aldrich) solution of 2.5×10^{-3} M was prepared in an alkaline medium using a carbonate buffer as a stock solution. Exactly, 60×10^{-6} M of morin was used to perform all the investigations. The morin adsorption and hydrogen peroxide stability during the reaction process were assured by using 1×10^{-3} M of carbonate buffer consisting of sodium carbonate (Merck laboratories, ≥98.0%) and sodium bicarbonate (Merck laboratories, ≥99.5%) maintaining the solution pH at 10. The mesoporous metal oxide slurry was mixed with morin solution and allowed to stir for 300 s. The desired amount of hydrogen peroxide (Merck laboratories, 30–35%) was added last to initiate the process. The hydrogen peroxide concentration was determined by titration [29]. Time intervals of 180 s were allocated to the reaction prior to the measurements. Deionized water from an in-house Milli-Q system (18 MΩ cm) was used to prepare all solutions.

Table 1
The synthesized mesoporous metal oxide materials physicochemical parameters.

MTMO	Initial color (150 °C)	Final color (450 °C)	Surface area (m² g⁻¹)	Pore size (nm)	Pore volume (cm³ g⁻¹)	Crystallite side (nm)	JCSD number
CeO₂	Yellow	Yellow	131.37	3.85	0.13	6.01	96-900-9009
NiO	Green	Dark-gray	44.11	21.89	0.24	14.97	96-101-0096
Co₃O₄	Brown	Black	21.23	28.41	0.15	20.22	96-900-5889
Fe₂O₃	Brown	Brown	32.31	23.65	0.19	34.41	96-101−1268
MnO₂	Brown	Black	22.81	22.16	0.12	24.64	96-900-7521
SiO₂	Yellow	White	548.03	1.99	0.27	1.18	96-900-6969

The catalytic investigation was conducted using a round bottom flask with a total volume of 30×10^{-3} L containing all the reactants. A volume of 3×10^{-3} L was collected from the solution mixture using a micro-pipette, and transferred into a quartz cuvette to perform the spectrophotometric analysis. The spectrum was scanned for the wavelength range of λ 600–230 nm, and the kinetics was followed at a fixed wavelength of λ 410 nm. The measurements were conducted using an UV–vis spectrophotometer (Shimadzu UV-1800 spectrophotometer).

3. Results and discussion

An acidified alcoholic solution of metal nitrate, heated to 120 °C, resulted in a powder consisting of the nitrate ion, carbonic ion, and metal oxide. The nitrate and the carbonate species were removed by heating the obtained powder to 150 °C. The first heating step (150 °C) technically removes the ionic species. Except for iron and cerium oxides, where the color did not change, the heat treatment of the remaining mesoporous metal oxide materials resulted in the color shifting from first heat treatment (150 °C) to final heat treatment (450 °C). The resulting color due to the heat treatment for each synthesized mesoporous material is given in Table 1. The mesoporous material mesostructure was investigated through electromagnetic radiation based on Braggs approach and revealed a couple of reflecting angles [30]. Fig. 1 shows the reflecting peaks detected through a low angle (A) and wide angle (B) analysis. A low and wide-angle XRD analysis demonstrated the crystallinity of the mesoporous metal oxide materials. The Scherrer equation was used to obtain the average crystallite size [31]. The Scherrer equation is given in Eq. 1S (see the Supporting information) and crystallite size of the mesoporous materials were deducted using a wide-angle XRD. The synthesized mesoporous materials identities were matched and obtained JSCD numbers are given in Table 1. The isotherm adsorption and desorption of nitrogen on the mesoporous metal oxide materials surface were conducted using Brunauer-Emmett-Teller approach [32,33]. The obtained surface area, pore volume, and pore diameter values are described in Table 1. The isotherm adsorption and pore-diameter plots are shown in Fig. 1(C–D). FT-IR analysis performed for all synthesized mesoporous metal oxide materials showed metal-oxygen bond (O—M—O) stretching vibration at the wavenumber range ν 489–891 cm⁻¹ [34]. FT-IR spectrum of the mesoporous materials is shown in Fig. 1S (see Supporting information).

A template approach was performed for the synthesis of encapsulated random alloy palladium-gold nanoparticles [35,36]. The amount of 1.13×10^{-4} and 5.25×10^{-5} mol of palladium and gold ions, respectively were added into the dendritic solution of 1.5×10^{-6} mol dendrimer. Both metal ions were reduced by an alkaline solution of sodium borohydride. The encapsulated random alloy nanoparticle solution was dialyzed overnight. The synthesis process was monitored using UV–vis spectroscopy which highlighted the formation of the alloy nanoparticles, demonstrating their corresponding absorbance peaks [26,37,38]. The UV–vis spectra are shown in Fig. 2S (A) (see Supporting information). The synthetic assumption is shown in Fig. 2. A high-resolution transmission electron microscopy analysis conducted on

Table 2
Percentage weight of metal nanoparticles immobilized on mesoporous metal oxide materials and TPR analysis results for the unsupported and supported metal oxide materials.

Mesoporous materials	% wt. of Pd	% wt. of Au	TPR Temperature (°C) First	Second
CeO₂	–	–	351	464
PdAu-CeO₂	0.030	0.054	186	402
NiO	–	–	341	–
PdAu-NiO	0.037	0.064	381	–
Co₃O₄	–	–	259	338
PdAu-Co₃O₄	0.036	0.062	159	310
Fe₂O₃	–	–	375	603
PdAu-Fe₂O₃	0.028	0.047	140	304
MnO₂	–	–	275	395
PdAu-MnO₂	0.034	0.059	147	339
SiO₂	–	–	–	–
PdAu-SiO₂	0.018	0.027	–	–

–: represents unsuccessful analysis of IC-OES or TPR.

random palladium-gold nanoparticle solution showed the well-dispersed nanoparticles. Their obtained average particle size is 2.66 ± 0.51 nm. The atomic ratio of palladium and gold solution were confirmed through EDS analysis. Fig. 2S (B–D) shows the micrograph (B), nanoparticles average size distribution (C), and EDS spectrum of the encapsulated random alloy palladium-gold nanoparticles (D), respectively (see Supporting information).

The terminal hydroxyl group of the dendrimer interacts with the mesoporous metal oxide materials by establishing a hydrogen bond [27,39]. A mixture of the encapsulated random alloy nanoparticle solution with the mesoporous metal oxide materials results in a colorless solution which demonstrates the interaction of dendrimer with a metal oxide material. A solution of 25×10^{-6} M (2×10^{-3} L) dendrimer encapsulated random alloy nanoparticles was mixed with the range of $(70–80) \times 10^{-3}$ g of mesoporous transition metal oxide materials. The mixture was subjected to sonication to improve the dispersion. The dendrimer template was thermally removed at 100 °C for 4 h. The weight percentage of palladium and gold nanoparticles loaded onto the metal oxide pores are shown in Table 2 The concentration of the encapsulated metal nanoparticles and the thermal removal of dendrimer influence quantitatively the metal nanoparticles loading on mesoporous metal oxide materials. A higher percentage of metal nanoparticles loaded on silica compared to this work was reported by Somorjai's group using 250×10^{-6} M of dendrimer concentration (0.3% of metal nanoparticles loaded) [27]. Thermal removing of dendrimer at 550 °C for 2 h reported by Zhou's group resulted in 1.5% of metal nanoparticles loaded on meso-ceria [40]. Here, a lower concentration of dendrimer or metal nanoparticles was used to assure the random alloy nanoparticles dispersion which improves their surface availability. Thermal removal of the dendrimer at a higher temperature may result in particle aggregation via surface diffusion which increases their diameter [39].

High-resolution transmission electron microscopy analysis performed on the synthesized mesoporous metal oxide materials
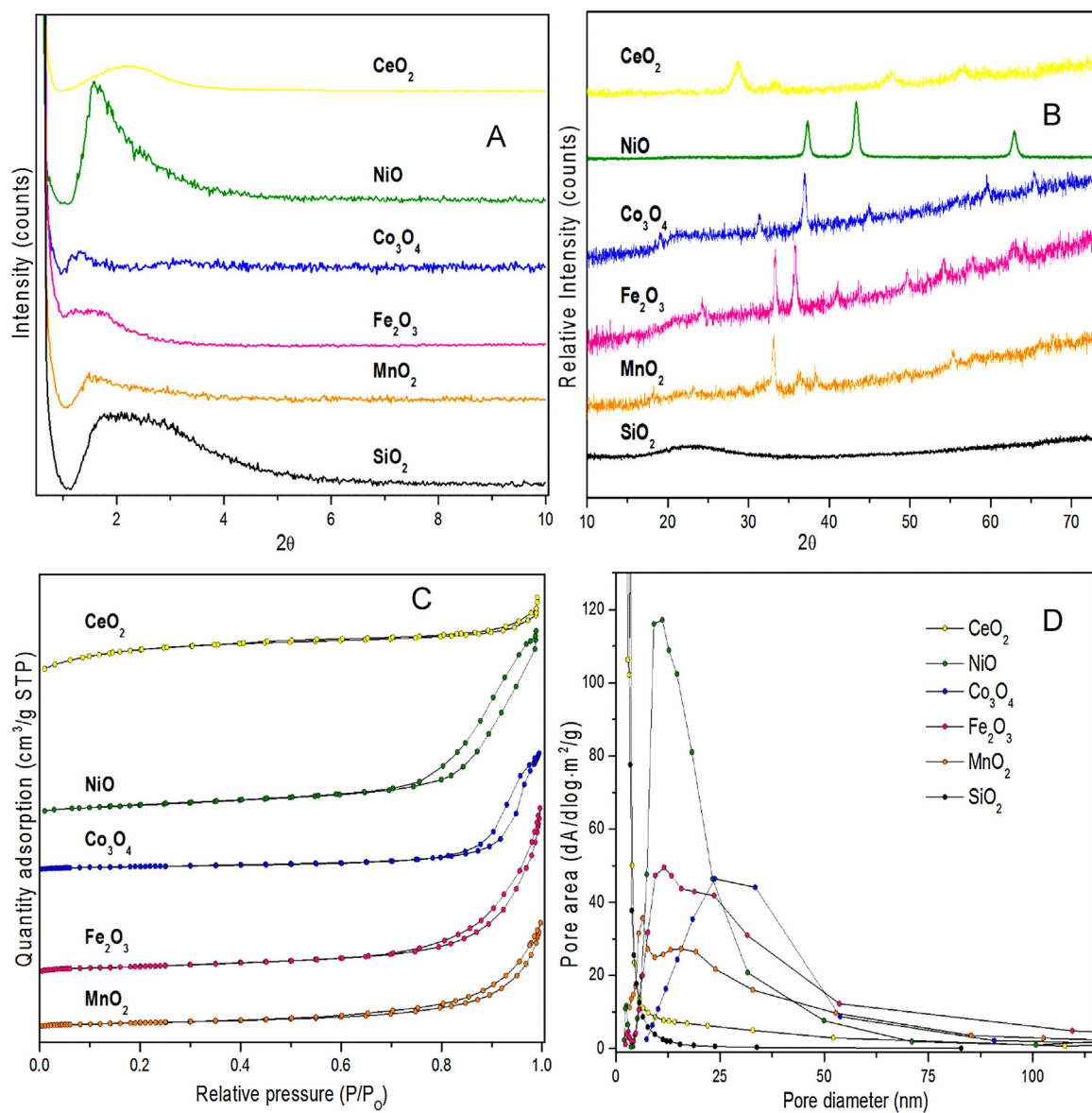
Fig. 1. (A) and (B) described an XRD analysis performed at a low and wide angle, respectively. Nitrogen isotherm adsorption and desorption analysis and pore-diameter are shown in (C) and (D), respectively.
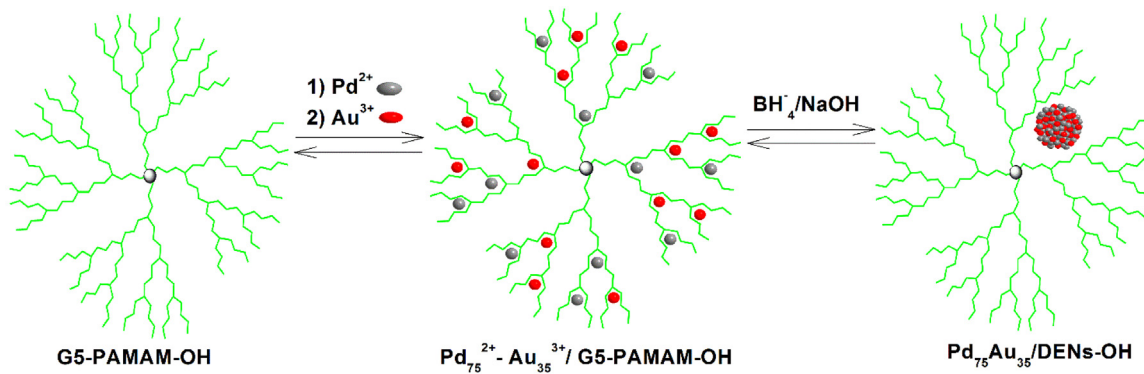

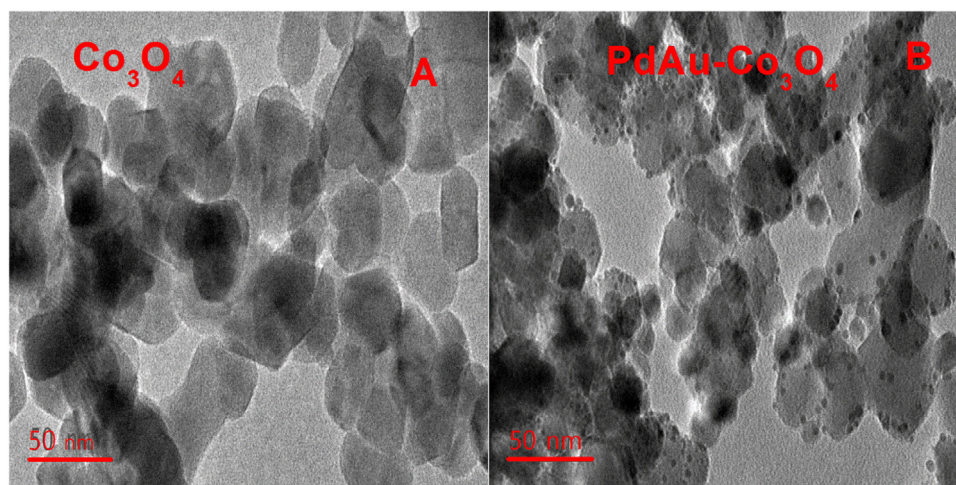**Fig. 2.** Synthesis scheme of the encapsulated random alloy nanoparticles.

Fig. 3. High-resolution transmission electron microscopy analysis of unsupported (A) and supported (B) cobalt oxide materials. (For interpretation of the references to color in the text, the reader is referred to the web version of this article.)
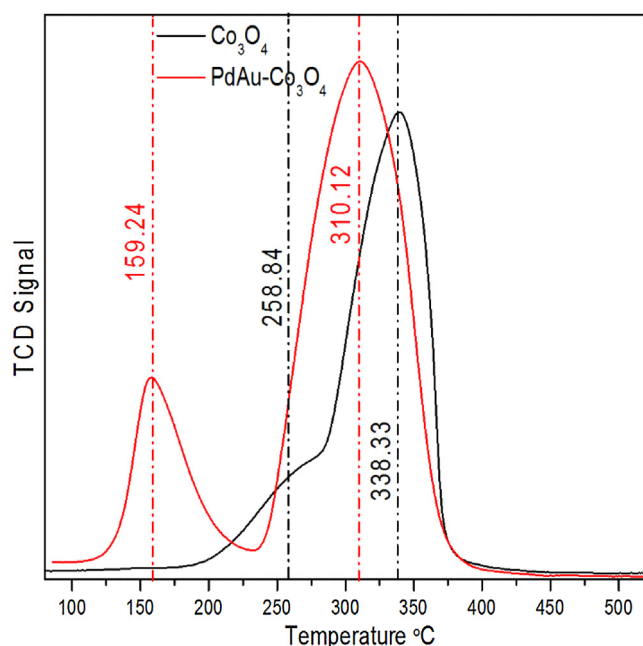

Fig. 4. TPR trace of Co_3O_4 versus $PdAu–Co_3O_4$.

Fig. 5. Morin structure.

shows the nanosized materials and demonstrated the crystalline structure of the metal oxides. The micrograph of cobalt oxides is shown in Fig. 3(A), for the remaining synthesized metal oxide materials, the micrographs are shown in Supporting information Fig. 3S(A–E). The immobilized metal nanoparticles onto mesoporous metal oxide materials show a narrow dispersion of the random alloy nanoparticles. HR-TEM image of palladium-gold nanoparticles immobilized on cobalt oxide materials is shown in Fig. 3(B). The micrographs of the remaining immobilized metal nanoparticle on mesoporous metal oxide materials are shown in the Supporting information (Fig. 4S (A–E)).

TPR analysis was performed using the MTMO and PdAu–MTMO materials. Shown in Fig. 4(A) is the cobalt oxide material only. The reduction peak shifted to a lower temperature for the alloy supported materials, which indicated the improvement in reducibility due to the interaction of metal nanoparticle and metal oxides. The reducibility resulting to the interaction of metal nanoparticle and metal oxide is related to the metal oxide applied. We detected that
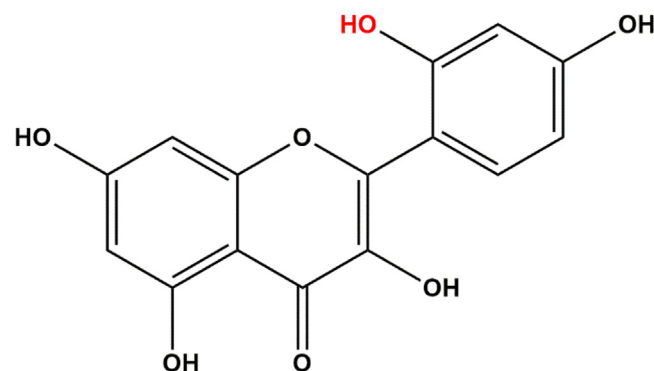
the immobilization of random alloy nanoparticle onto mesoporous nickel oxide resulted in a peak shift to a higher temperature. TPR analysis of the other composites is shown in the Supporting information (Fig. 5S (A–E)). PdAu–SiO$_2$ showed no reduction peak, which indicated the inactivity of silica and the thermal stability of metal nanoparticles. Table 2 gives the TPR results for the unsupported and supported metal oxide materials.

Catalytic oxidation of morin was conducted as a model reaction for two reasons. First, as a quercetin compound, morin undergoes the oxidation process easily, and secondly, the ortho-position of the hydroxyl group R$_1$ prevents the process of morin dimerization [24,25]. The morin structure is shown in Fig. 5 and the ortho-positioned hydroxyl group is highlighted in red. The catalytic processes were performed in alkaline medium because the morin absorbance is related to the pH [41]. The catalytic oxidation was monitored using spectrophotometry at λ 410 nm which is the maximum absorption peak for the model compound (morin). The uncatalyzed oxidation of morin in the presence of hydrogen peroxide was performed, which resulted in a low oxidation rate. The minimal reactivity is ascribed to the interaction of hydrogen peroxide with the carbonate to form the peroxycarbonate ion [42]. Morin oxidation leads to the formation of two types of benzoic acids which can undergo a further degradation [25]. The morin degradation mechanism was suggested in our previous report based on liquid chromatographic analysis [43]. The secondary peaks observed at λ 317 and λ 273 nm are related to the formed products and their further decomposition [25]. The reaction product formation and their further decomposition can be monitored through UV–vis
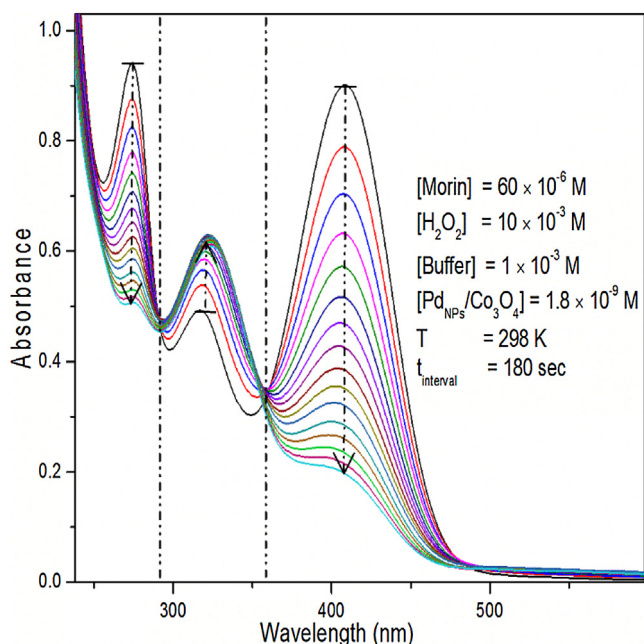
Fig. 6. UV–vis spectrum of morin oxidation catalyzed by PdAu–Co$_3$O$_4$.

spectroscopy which shows two isosbestic points. UV–vis spectrum is shown in Fig. 6 for PdAu–Co$_3$O$_4$ used as a catalyst. The isosbestic point detected through manganese oxide run was permanently occurring at all oxidation processes compared to the other metal oxide materials which described a temporary isosbestic point (see Supporting information (Fig. 6S)).

The reaction was carried out at 25 °C where exactly, 60×10^{-6} M of morin and 10×10^{-3} M of hydrogen peroxide were contained in 30×10^{-3} L of deionized water. Considering the large concentration of hydrogen peroxide used, the reaction shows *pseudo*-first order behavior [44]. The uncatalyzed and catalyzed process over time using PdAu–Co$_3$O$_4$ as catalyst are shown in Fig. 7. Morin oxidation over time using an increasing concentration of palladium nanoparticle immobilized onto cobalt oxide is shown in Fig. 7(A), where the corresponding reaction order is shown in Fig. 7(B).

Mesoporous metal oxide materials were used as a catalyst in some catalytic reactions that can be explained by their electronic state which shows multiple oxidation states [12,45–48]. In the light of those reports, all the synthesized mesoporous metal oxide

materials were used as a catalyst for morin oxidation to evaluate their catalytic ability in the presence of hydrogen peroxide. Nickel, cobalt, and manganese oxide materials show catalytic activity, however, cerium, iron, and silica did not show activity. The observed rate constant versus the metal oxide materials surface area for those active mesoporous materials are shown in the Supporting information (Fig. 7S). The observed rate constant describes a linear relationship which indicates that the reaction rate increases proportionally with the surface area. The red star points in Fig. 7S show the zone where the observed rate constant cease to establish a linear relationship with the mesoporous surface area.

The composite of PdAu–MTMO was subjected to catalytic evaluation through the model reaction (morin oxidation). The use of PdAu–MTMO as a catalyst consist in the determining synergistic interaction of metal nanoparticles and metal oxide materials. To isolate the metal nanoparticles catalytic ability, silica was used as an inert support [44]. The observed inactivity of SiO$_2$ through the model reaction, support its role as inert support. All the composite materials (PdAu–MTMO) show a catalytic activity, which indicates an excellent synergistic interaction of PdAu and MTMO. The observed rate constant versus the concentration of palladium nanoparticle on mesoporous materials plots is shown in Fig. 8(A–F). PdAu–Co$_3$O$_4$ and PdAu–SiO$_2$ demonstrated a continuing linear relationship between the observed rate constant and the palladium nanoparticle concentration, however, the rest (PdAu–NiO, PdAu–Fe$_2$O$_3$, PdAu–CeO$_2$, and PdAu–MnO$_2$) shows an optimum palladium nanoparticle concentration highlighted with the red star. The red star on Fig. 8 describe the zone where the observed rate constant ceases to linearly increase with palladium nanoparticle amount on mesoporous metal oxide materials.

The catalytic process was performed under aerobic conditions which may result in interference by oxygen. The amount of active metal oxide materials and Pd nanoparticle concentration on mesoporous metal oxide materials highlighted as the green star in Fig. 7S and Fig. 8 were taken as a catalyst concentration through a model reaction using oxygen as an oxidant to evaluate the oxygen interference. The observed rate constants were ten times lower $((5.52 \pm 0.01) \times 10^{-5}$ (s^{-1})), ten times lower $((2.72 \pm 0.01) \times 10^{-5}$ (s^{-1})) and three times lower $((2.56 \pm 0.01) \times 10^{-4}$ (s^{-1}) using NiO, Co$_3$O$_4$, and MnO$_2$, respectively as catalysts. No oxygen interference was detected with the immobilized palladium-gold nanoparticles on mesoporous materials as a catalyst, which demonstrates the highest activity of the metal nanoparticles.

The reusability of the random alloy on mesoporous metal oxide materials was evaluated through three cyclic runs. The catalyst
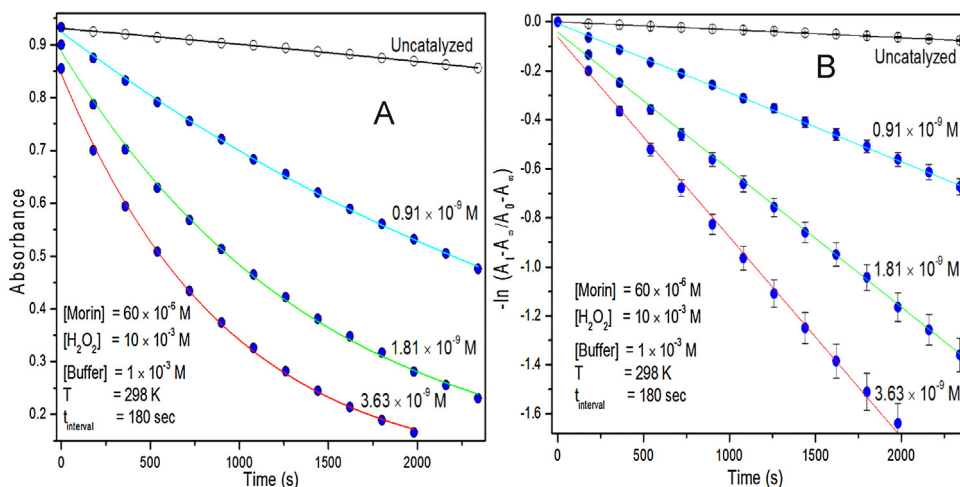

Fig. 7. Morin oxidation process (A) and the corresponded reaction *pseudo*-first order plots (B) over time using PdAu–Co$_3$O$_4$ as a catalyst.
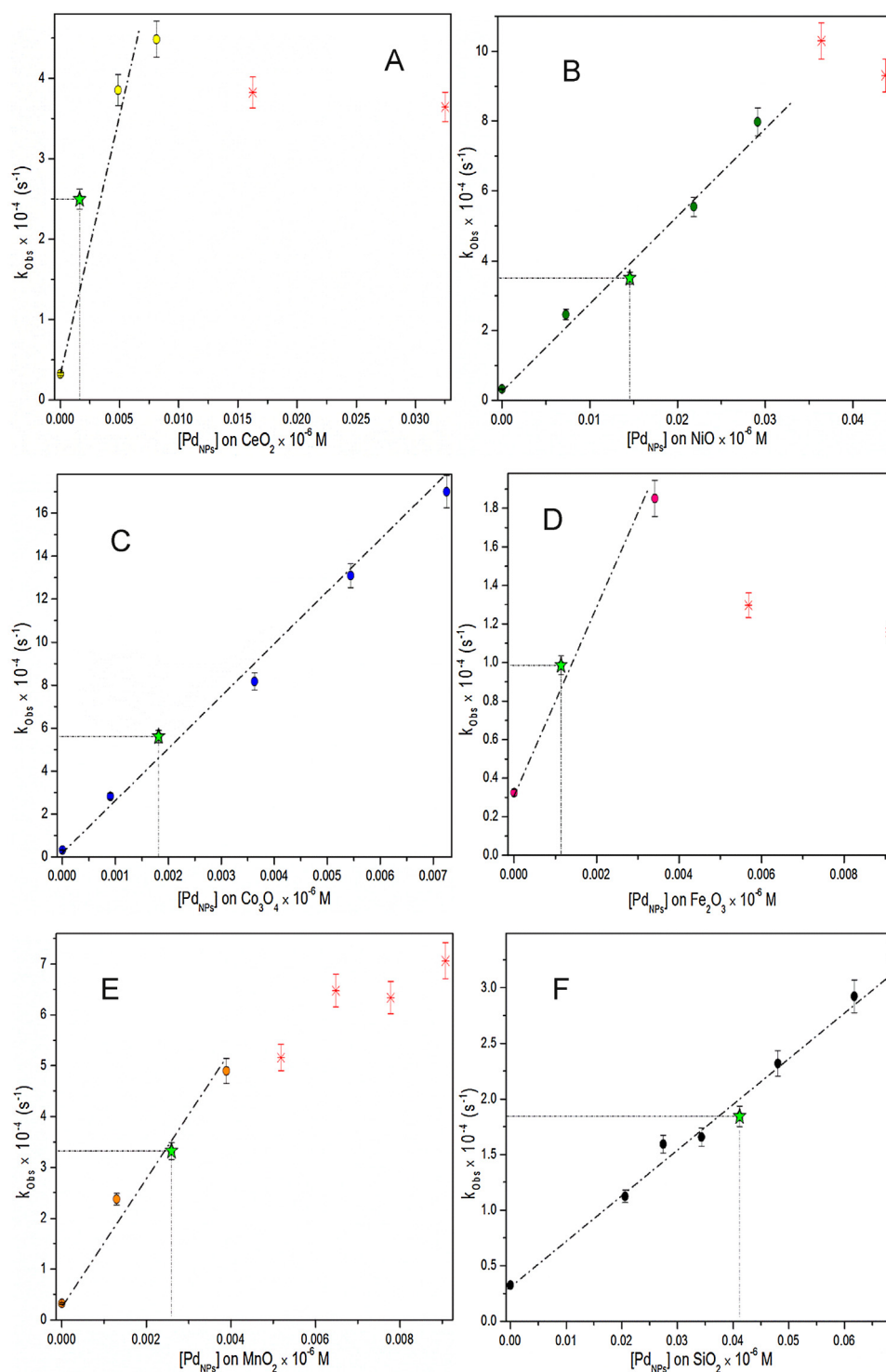
Fig. 8. (A–F) Plots of the concentration of palladium nanoparticle immobilized onto mesoporous metal oxide materials versus the observed rate constant. (For interpretation of the references to color in the text, the reader is referred to the web version of this article.)

recovery was performed by centrifugation and rinsed with a large volume of deionized water. Only PdAu-Co$_3$O$_4$ was subjected to the reusability investigation which demonstrated its stability during the catalytic process. The observed rate constant, k$_{obs}$, calculated for the three recycle runs are 6.32×10^{-4} s^{-1}, 3.66×10^{-4} s^{-1}, and 2.53×10^{-4} s^{-1} from the initial to the final run. The activity of the recycled catalyst is shown in Fig. 9(A). Due to the very small mass of catalyst used, its recovery from the resulting products and purification prior to the next run impacted significantly on the activity

of the catalyst. The micrograph of PdAu–Co$_3$O$_4$ shown in Fig. 9(B) demonstrated that the catalyst was virtually unchanged after three catalytic runs.

The reaction rate was normalized on Pd concentration of the palladium-gold nanoparticles immobilized on mesoporous metal oxide materials and expressed as turnover frequency are reported in Fig. 10(A). TOF were calculated at 298 K for each green star shown in Fig. 7S and Fig. 8 for the pure metal oxide and the immobilized metal nanoparticles on metal oxide materials. The TOF described
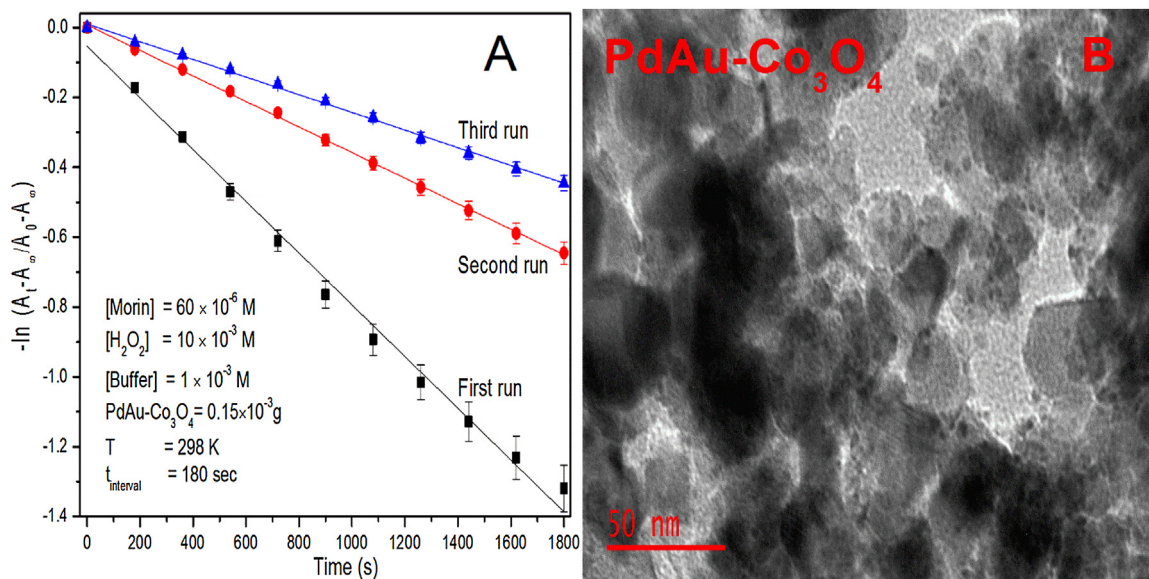
Fig. 9. Reusability of PdAu-Co_3O_4 through a cyclic run (A) and micrograph taken after cyclic run (B).
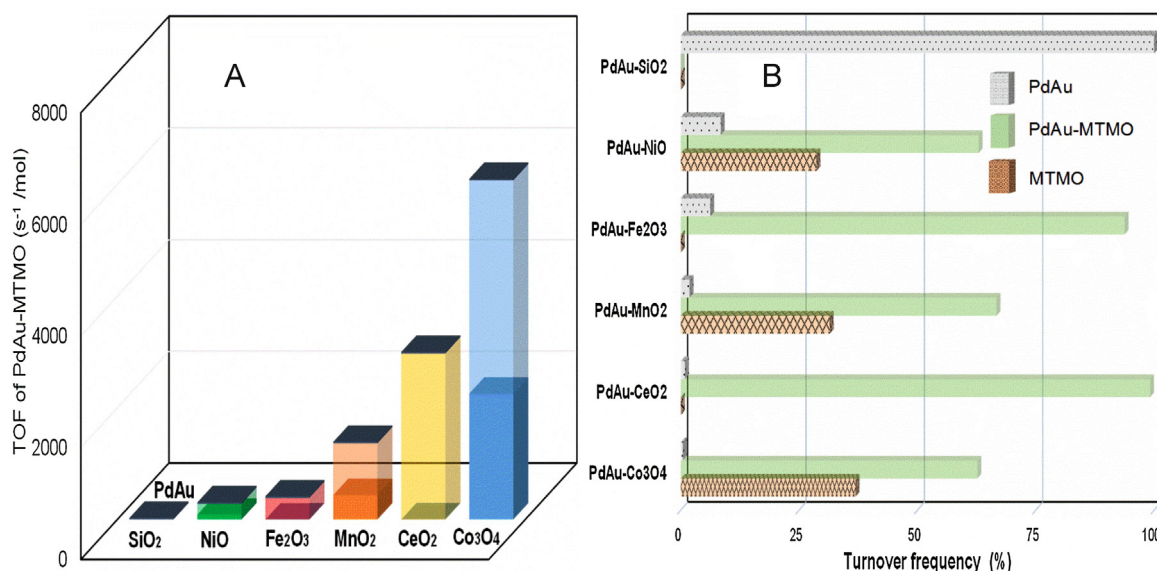

Fig. 10. TOF plots of MTMO and PdAu–MTMO (A), and TOF value in percentage (B).

Table 3
Normalized reaction rate (TOF) and activity of the immobilized metal nanoparticles onto mesoporous metal oxide materials through morin oxidation.

PdAu–MTMO	TOF at 298 K ($s^{-1}\,mol^{-1}$)	Activity ($kJ\,mol^{-2}$)
PdAu–CeO_2	2973.10 ± 35.14	67.04 ± 1.57
PdAu–NiO	278.86 ± 18.95	41.37 ± 8.92
PdAu–Co_3O_4	6073.23 ± 85.01	71.12 ± 8.55
PdAu–Fe_2O_3	386.72 ± 36.02	61.13 ± 2.63
PdAu–MnO_2	1363.21 ± 65.32	61.32 ± 10.33
PdAu–SiO_2	25.71 ± 2.35	32.69 ± 9.93
$Pd_{75}Au_{35}$/DENs-OH		$(34.78 \pm 4.35)\,kJ\,mol^{-1}$

by PdAu–MTMO is significantly larger compared to that described by MTMO. The calculated TOF of immobilized palladium-gold alloy nanoparticles onto mesoporous metal oxide materials are reported in Table 3. The synergistic interaction of metal-support considerably increases the formation of active species which improve the oxidation process. The random alloy nanoparticles catalytic activ-

ity was isolated through supporting on silica. The TOF described by PdAu–SiO_2 is related to the metal alloy nanoparticles that highlighted random palladium-gold alloy nanoparticles catalytic activity through the model reaction.

The isolated TOF value of metal nanoparticles, metal oxide materials, and the metal-support interaction expressed in percentage are shown in Fig. 10(B). The TOF of PdAu–CeO_2 and PdAu–Fe_2O_3 are over 90% resulting from synergistic interaction between metal nanoparticles and metal oxide materials. The synergistic interaction of PdAu–NiO, PdAu–Co_3O_4, and PdAu–MnO_2 contributed at 60% of TOF value. The TOF value in percentage described by active mesoporous metal oxide materials are increasing as that 37%, 31%, and 29% for Co_3O_4, MnO_2, and NiO, respectively. TOF value of PdAu–SiO_2 is 100% due to the metal nanoparticle activity. Cobalt oxide material shows a higher percentage of isolated TOF value which demonstrated its excellent reducibility.

The metal nanoparticles catalytic activity were mechanically described using Langmuir-Hinshelwood approach which defined
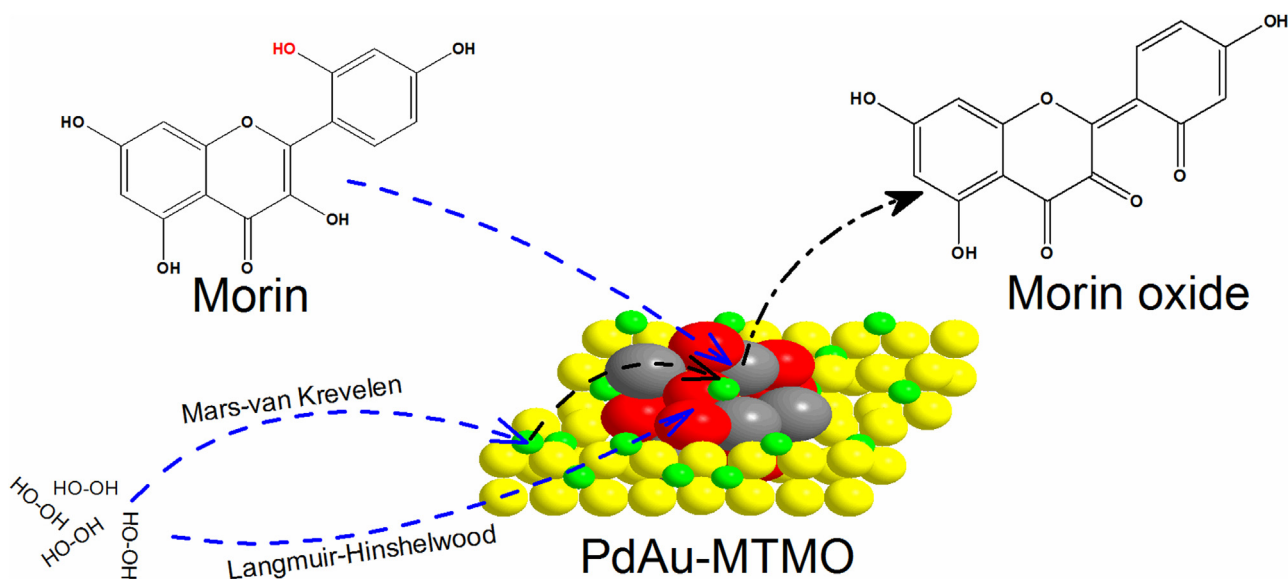
Fig. 11. Combination of Langmuir-Hinshelwood and Mars-van Krevelen mechanism.

the catalyst as a platform consist of the active sites where the reactants adsorbed, prior to the reaction forming the product species [18]. The hydrogen peroxide adsorbed on a metal nanoparticle surface to form a hydroxide radical which is a higher potential. Comparative TPR analysis results of unsupported and supported mesoporous metal oxide materials indicated the reducibility of the synthesized mesoporous metal oxide materials. The reducibility of the catalyst can be described as oxygen species being released from the metal oxide materials. The free oxygen species acted as oxidant agent that can mechanically be investigated according to the Mars-van Krevelen approach [49]. The synergistic effect of metal oxide and metal nanoparticle consist of two sources of oxidant agent formations that dramatically increase the catalytic oxidation process.

No interference by oxygen is observed using PdAu–MTMO as a catalyst. This is attributed to the formation of a higher potential oxidant (hydrogen peroxide) which considerably accelerates the process. The synergistic interaction between the metal oxide and metal nanoparticle involves the combining of Langmuir-Hinshelwood and Mars-van Krevelen approach. The combination of the Langmuir-Hinshelwood and Mars-van Krevelen mechanisms is illustrated in Fig. 11. PdAu–NiO shows a lower TOF compared to the other reducible metal oxide. That can be explained regarding TPR result of PdAu–NiO which indicates reducibility at a higher temperature compared to NiO. The supporting of metal nanoparticle on ceria and iron oxide shifted their reduction temperature which results in a good catalytic performance compared to the inactive ceria and iron oxides materials. PdAu–Co$_3$O$_4$ shows a higher TOF which confirms the reducibility of Co$_3$O$_4$ and the synergic effect of the composite.

The activity of the catalyst was investigated at three temperatures namely 283, 293, and 303 K. Catalytic process consist of the formation of active species which oxidize morin to morin oxide. Morin oxide undergoes a further systematic degradation [18]. The synergistic interaction of metal-support was reported for CO-hydrogenation and the metal activity was isolated by supporting on silica [50]. The Arrhenius-type plot of TOF versus the temperature was constructed to obtain the activity, it is fundamental to notice that the higher activity corresponds to higher value [50,51]. The palladium nanoparticle concentration highlighted at the green star on Fig. 8 was applied as catalyst amount for temperature influence study. PdAu–NiO shows a lower activity compared to

the active reducible metal oxide materials which can be attributed to poor reducibility of nickel oxide. PdAu–Co$_3$O$_4$ described the highest activity which indicated the great synergistic interaction of the composite improving the release of active species. The activity described by the composite PdAu–MTMO is fundamentally due to the synergistic interaction of the metal oxide and metal nanoparticles. The reducibility of the metal oxide materials depends on the physicochemical parameters of reaction [52]. Fig. 8S shown in the Supporting information described the Arrhenius-type plot constructed for PdAu–MTMO. The activity of immobilized metal nanoparticles onto mesoporous metal oxide materials is shown in Table 3. The activity demonstrated using PdAu–SiO$_2$ corresponded to those of random palladium-gold nanoparticles. The activity of PdAu–SiO$_2$ shows a similar value with the activation energy calculated using the observed rate constant for Pd$_{75}$Au$_{35}$/DENs-OH (34.78 kJ mol^{-1}) [18].

4. Conclusion

Well-dispersed random palladium-gold nanoparticles synthesized by template method using dendrimer were immobilized onto mesoporous metal oxide materials. The synthesized mesoporous metal oxide materials were applied as metal nanoparticle support. Morin oxidation was performed as a model reaction in the presence of hydrogen peroxide as an oxidant to investigate the synergistic interaction of metal nanoparticles and metal oxide materials. Silica was used as inert support to isolate the catalytic ability of random alloy nanoparticles. The reducibility of metal oxide materials which represented a great advantage in their contribution in catalytic oxidation process was analyzed by TPR analysis. PdAu–NiO demonstrated a poor reducibility compared to the remaining synthesized PdAu–MTMO materials. TOF values described by PdAu–MTMO were considerably large compared to which described by metal nanoparticle (over 230 times larger). The combining of Langmuir-Hinshelwood and Mars-van Krevelen approaches were considered as a catalytic mechanism. The interaction of reactant onto the metal nanoparticle surface represented the rate determinating for active species formation (Langmuir-Hinshelwood) and the reducibility of metal oxide which leads to the oxygen molecule releasing consisting of an oxidizing agent source (Mars-van Krevelen). The activity of random alloy nanoparticles was 32.69 kJ mol^{-2} which is similar to the activity obtained for colloidal random alloy nanoparticles

$(34.78 \, kJ \, mol^{-1})$. PdAu–$Co_3O_4$ demonstrated the best synergist catalytic combination followed by PdAu–CeO_2.

Acknowledgements

Appendix A. Supplementary data

Supplementary data associated with this article can be found, in the online version, at http://dx.doi.org/10.1016/j.apcatb.2016.10.053.

References

[1] J.S. Beck, J.C. Vartuli, W.J. Roth, M.E. Leonowicz, C.T. Kresge, K.D. Schmitt, C.T.-W. Chu, D.H. Olson, E.W. Sheppard, S.B. McCullen, J.B. Higgins, J.L. Schlenkert, J. Am. Chem. Soc. (1992) 10834–10843.
[2] C.T. Kresge, M.E. Leonowicz, W.J. Roth, J.C. Vartuli, J.S. Beck, Nature 359 (1992) 710–712.
[3] C. Liang, S. Dai, J. Am. Chem. Soc. 128 (2006) 5316–5317.
[4] B.G. Trewyn, I.I. Slowing, S. Giri, H.T. Chen, V.S. Lin, Acc. Chem. Res. 40 (2007) 846–853.
[5] L.F. Chen, X.D. Zhang, H.W. Liang, M. Kong, Q.F. Guan, P. Chen, Z.Y. Wu, S.H. Yu, ACS Nano 6 (2012) 7092–7102.
[6] L. Huang, W. Guo, P. Deng, Z. Xue, Q. Li, J. Phys. Chem. B 104 (2000) 2817–2823.
[7] H. Li, Z. Bian, J. Zhu, D. Zhang, G. Li, Y. Huo, H. Li, Y. Lu, J. Am. Chem. Soc. 129 (2007) 8406–8407.
[8] G.S. Chai, S.B. Yoon, J.S. Yu, J.H. Choi, Y.E. Sung, J. Phys. Chem. B 108 (2004) 7074–7079.
[9] T.F. Degnan, Stud. Surf. Sci. Catal. 170 (2007) 54–65.
[10] J. Fan, C. Yu, F. Gao, J. Lei, B. Tian, L. Wang, Q. Luo, B. Tu, W. Zhou, D. Zhao, Angew. Chem. 115 (2003) 3254–3258.
[11] H. Li, Z. Bian, J. Zhu, D. Zhang, G. Li, Y. Huo, H. Li, Y. Lu, J. Am. Chem. Soc. 129 (2007) 8406–8407.
[12] Z. Tian, Science 276 (1997) 926–930.
[13] D. Grosso, F. Cagnol, G.J.D.A.A. Soler-Illia, E.L. Crepaldi, H. Amenitsch, A. Brunet-Bruneau, A. Bourgeois, C. Sanchez, Adv. Funct. Mater. 14 (2004) 309–322.
[14] B. Tian, X. Liu, B. Tu, C. Yu, J. Fan, L. Wang, S. Xie, G.D. Stucky, D. Zhao, Nat. Mater. 2 (2003) 159–163.
[15] A.S. Poyraz, C.-H. Kuo, S. Biswas, C.K. King'ondu, S.L. Suib, Nat. Commun. 4 (2013) 2952.
[16] K. Mudiyanselage, J.F. Weaver, J. Szanyi, J. Phys. Chem. C 115 (13) (2011) 5903–5909.
[17] F. Garin, Appl. Catal. A Gen. 222 (2001) 183–219.
[18] A.K. Ilunga, R. Meijboom, Appl. Catal. B Environ. 189 (2016) 86–98.
[19] S. Alayoglu, K. An, G. Melaet, S. Chen, F. Bernardi, L.W. Wang, A.E. Lindeman, N. Musselwhite, J. Guo, Z. Liu, M.a. Marcus, G.a. Somorjai, J. Phys. Chem. C 117 (2013) 26608–26616.
[20] K. An, S. Alayoglu, N. Musselwhite, S. Plamthottam, G. Melaet, A.E. Lindeman, G.A. Somorjai, J. Am. Chem. Soc. 135 (2013) 16689–16696.
[21] S. Biswas, A.S. Poyraz, Y. Meng, C.H. Kuo, C. Guild, H. Tripp, S.L. Suib, Appl. Catal. B Environ. 165 (2015) 731–741.
[22] R. Jain, A.S. Poyraz, D.P. Gamliel, J. Valla, S.L. Suib, R. Maric, Appl. Catal. A Gen. 507 (2015) 1–13.
[23] A.Y. Waddad, S. Abbad, F. Yu, W.L.L. Munyendo, J. Wang, H. Lv, J. Zhou, Int. J. Pharm. 456 (2013) 446–458.
[24] S. Rothbart, E. Ember, R. van Eldik, Dalt. Trans. (Cambridge, Engl. 2003) 39 (2010) 3264–3272.
[25] F. Polzer, S. Wunder, Y. Lu, M. Ballauff, J. Catal. 289 (2012) 80–87.
[26] M.G. Weir, M.R. Knecht, A.I. Frenkel, R.M. Crooks, Langmuir 26 (2010) 1137–1146.
[27] W. Huang, J.N. Kuhn, C.K. Tsung, Y. Zhang, S.E. Habas, P. Yang, G.A. Somorjai, Nano Lett. 8 (2008) 2027–2034.
[28] N. Hayashi, Y. Sakai, H. Tsunoyama, A. Nakajima, Langmuir 30 (2014) 10539–10547.
[29] B. Cornish, L.A. Lawton, P.K.J. Robertson, Appl. Catal. B Environ. 25 (2000) 59–67.
[30] L. Tarnawska, A. Giussani, P. Zaumseil, M.A. Schubert, R. Paszkiewicz, O. Brandt, P. Storck, T. Schroeder, J. Appl. Phys. 108 (2010).
[31] A. Monshi, M.R. Foroughi, M.R. Monshi, World J. Nano Sci. Eng. 2 (2012) 154.
[32] L. Chen, Y. Honsho, S. Seki, D. Jiang, J. Am. Chem. Soc. 132 (2010) 6742–6748.
[33] K.Y. Foo, B.H. Hameed, Chem. Eng. J. 156 (2010) 2–10.
[34] L. Gao, J. Sun, Y. Li, J. Solid State Chem. 184 (2011) 1909–1914.
[35] R.M. Crooks, M. Zhao, L. Sun, V. Chechik, L.K. Yeung, Acc. Chem. Res. 34 (2001) 181–190.
[36] Y. Liu, J. Goebl, Y. Yin, Chem. Soc. Rev. 42 (2013) 2610–2653.
[37] R.W.J. Scott, O.M. Wilson, S.-K. Oh, E.A. Kenik, R.M. Crooks, J. Am. Chem. Soc. 126 (2004) 15583–15591.
[38] Y.G. Kim, S.K. Oh, R.M. Crooks, Chem. Mater. 16 (2004) 167–172.
[39] L. Sun, R.M. Crooks, Langmuir 18 (2002) 8231–8236.
[40] Q. Wang, Y. Zhang, Y. Zhou, Z. Zhang, J. Xue, Y. Xu, C. Zhang, X. Sheng, N. Kui, RSC Adv. 6 (2016) 730–739.
[41] T. Wieprecht, U. Heinz, J. Xia, G. Schlingloff, J. Dannacher, J. Surf. Deterg. 7 (2004) 59–66.
[42] S. Rothbart, E. Ember, R. Van Eldik, Dalton Trans. 2 (2010) 3264–3272.
[43] A.K. Ilunga, R. Meijboom, Appl. Catal. A Gen. 509 (2016) 17–29.
[44] A.A. Osunlaja, S.O. Idris, J.F. Iyun, Arch. Appl. Sci. Res. 4 (2012) 772–780.
[45] R. Hamid, Nano-Micro Interface, Wiley Blackwell, 2005, pp. 139–150.
[46] Y. Shen, D. Zheng, B. Yang, S. Ni, S. Zhu, J. Rare Earth 30 (2012) 431–436.
[47] M. Besson, P. Gallezot, Catal. Today 57 (2000) 127–141.
[48] M.E. Dry, Catal. Today 71 (2002) 227–241.
[49] A.M. Khenkin, R. Neumann, Angew. Chem. 39 (2000) 4088–4090.
[50] M.A. Vannice, J. Mol. Catal. 59 (1990) 165–177.
[51] D. Samantaray, S. Mandal, A.K. Bhaduri, Comput. Mater Sci. 47 (2009) 568–576.
[52] K. Chen, A.T. Bell, E. Iglesia, J. Phys. Chem. B 104 (2000) 1292–1299.